Doping dependence of the contact resistivity of end-bonded metal contacts to thin heavily doped semiconductor nanowires

Anvar A. Shukkoor, and Shreepad Karmalkar

Citation: Journal of Applied Physics **122**, 214501 (2017);
View online: https://doi.org/10.1063/1.4991542
View Table of Contents: http://aip.scitation.org/toc/jap/122/21
Published by the American Institute of Physics

Doping dependence of the contact resistivity of end-bonded metal contacts to thin heavily doped semiconductor nanowires

Anvar A. Shukkoor[a] and Shreepad Karmalkar[b]
Department of Electrical Engineering, Indian Institute of Technology Madras, Chennai, Tamil Nadu 600036, India

(Received 21 June 2017; accepted 8 November 2017; published online 5 December 2017)

We study the resistivity, ρ_{cN}, of end-bonded contacts to semiconductor NanoWires (NWs) of radius $R = 5$–10 nm over doping $N_d = 10^{18}$–10^{20} cm^{-3}. The study is important for NW device design and characterization. It reports realistic calculations of ρ_{cN} and highlights and explains how ρ_{cN} differs significantly from the resistivity ρ_{cB} of bulk contacts. First, the space-charge width in NW contacts is increased by the surrounding field which depends on R, contact geometry, and ambient dielectric; this width also depends on surface charge and dielectric confinement which reduces dopant ionization. Second, thin NWs have a low effective lifetime, τ_N, due to surface recombination. Third, NW contacts have a lesser image force barrier lowering due to the higher space-charge width. Due to these factors, apart from tunneling (which decides ρ_{cB}), space-charge region generation-recombination current also affects ρ_{cN}. As N_d is raised from 10^{18} to 10^{20} cm^{-3}, ρ_{cB} falls rapidly, but ρ_{cN} varies slowly and may even increase up to 3–5×10^{18} and then falls rapidly. Further, ρ_{cN}/ρ_{cB} can be $\ll 1$ at $N_d = 1 \times 10^{18}$ cm^{-3}, reaches a peak $\gg 1$ around $N_d = 1 \times 10^{19}$ cm^{-3}, and $\rightarrow 1$ at $N_d = 1 \times 10^{20}$ cm^{-3}, e.g., for 0.8 V contact barrier on 10 nm thick n-type silicon NWs with $\tau_N = 1$ ps embedded in SiO_2, at $T = 300$ K, even a 10 nm contact extension yields a peak of 75 at $N_d = 8 \times 10^{18}$ cm^{-3}. We study changes in ρ_{cN}/ρ_{cB} versus N_d behavior with R, contact geometry, ambient dielectric, surface charge, τ_N, T, tunneling mass, and barrier height. *Published by AIP Publishing.* https://doi.org/10.1063/1.4991542

I. INTRODUCTION

Today, devices are being fabricated in semiconductor NanoWires (NWs) to harness unique properties arising from the high surface to volume ratio of NWs. During their operation and characterization, NW devices communicate with the outside world through metal contacts, whose resistivity affects NW device characteristics. The subject of the present paper is the resistivity of an *end-bonded*[1] metal contact [see Fig. 1(a)] which occurs in some NW devices and in characterization of single or arrays of NWs.[2–7] The radial extension, L_E, of the contact represents the effective metal electrode[8] over a NW of an array or a probe tip contacting a single NW; the cylindrical protrusion, L_P, represents[3] a possible metallic nano-particle between the NW and the contact or metal penetration into the NW. Other parameters of the contact are radius R and doping N_d of the NW, permittivity ε_s (ε_a) of the NW (ambient dielectric), and surface defects which cause a charge Q_S[9–11] and surface recombination velocity, s.

The high surface to volume ratio of a NW has major influences on two features of the NW contact, namely, the effective lifetime, τ_N, and the space-charge width defined as the distance from the contact where the space-charge drops to 50% of the ionized dopant charge at the contact. The effect of s gets magnified[3] causing τ_N to be orders of magnitude lower than the bulk lifetime, τ_B. The space-charge width gets decided not only by the field within the NW but also by: (a) the surrounding field line[4,12] setup on the NW surface by the metal contact; (b) dielectric confinement[13–15] of dopants (due to $\varepsilon_a < \varepsilon_s$) that reduces ionization of the dopant by raising its ionization energy; (c) NW surface charge Q_S.[9–11] It is known[4,8,12,16] that the surrounding field, which depends on R, L_E, L_P, ε_s, and ε_a, increases the space-charge width of the NW contact over that of the bulk contact [see Figs. 1(a) and 1(b)]. This space-charge width is further enhanced by dielectric confinement and a Q_S of polarity opposite to that of ionized dopants. The surrounding field and Q_S cause the space-charge width to be non-uniform over the NW cross-section.

The space-charge width correlates directly with the "generation-recombination width" or "GR width" associated with space-charge region GR current, I_{GR}, and "barrier width" associated with tunneling current, I_T. Here, "GR width" refers to the portion of the space-charge region, where the pn product deviates from the square of the intrinsic concentration[17] and "barrier width" refers to the portion of the space-charge region where most of the potential drop occurs. A NW contact has a long space-charge tail[8,12] beyond the space-charge width defined as per the above 50% criterion. However, this tail does not contribute to either the GR width or the barrier width.

Refer to Fig. 1(c). On account of $\tau_N \ll \tau_B$ coupled with a higher space-charge width, a NW contact has significant, I_{GR},[2,3,18] compared to the bulk contact. On the other hand, the higher space-charge width lowers the tunneling current, I_T, of the NW contact below that of a bulk contact;[4] here, I_T includes Thermionic Field Emission (TFE) and Field

[a]Author to whom correspondence should be addressed: anvar9101987@gmail.com
[b]Electronic mail: karmal@ee.iitm.ac.in

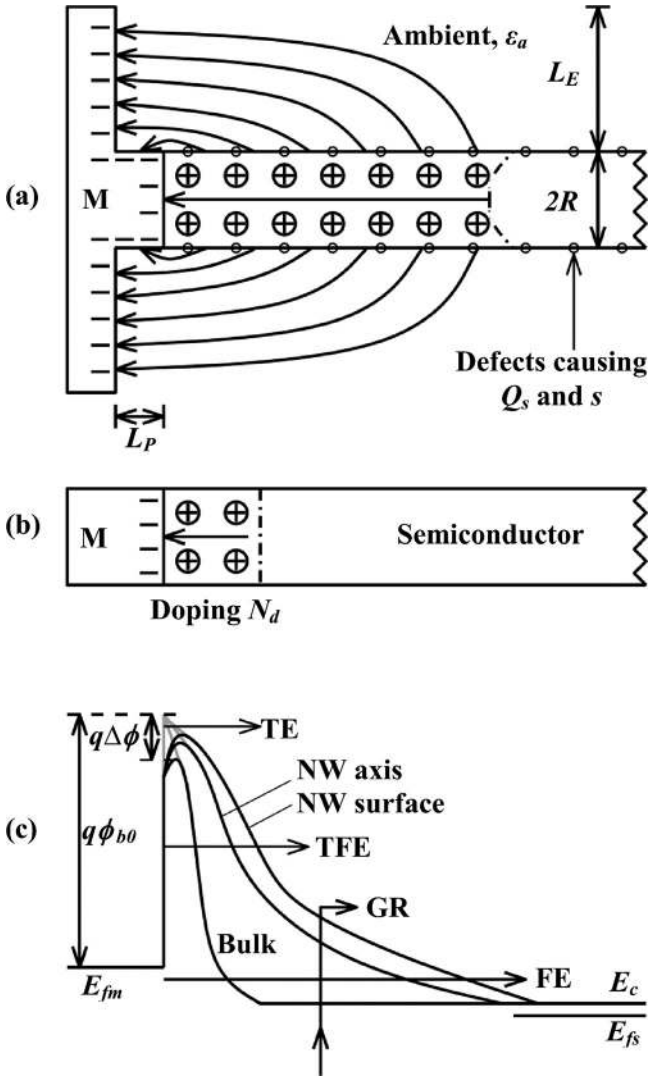

FIG. 1. Differences in factors affecting the resistivity of NW and bulk contacts. (a) Charges, field lines, and surface defects in a metal contact to an n-type semiconductor nanowire. (b) Charges and field lines in a bulk contact having the same doping and cross-section as the nanowire. The absence of the surrounding field and surface charge of (a) lead to a smaller space-charge width with a flat edge. (c) Conduction band (E_c) profiles of bulk and NW junctions and the mechanisms of electron emission/generation at small reverse bias. The bulk contact has negligible GR current due to the absence of surface defects. The NW contact has a smaller image force barrier lowering $\Delta\phi$ than the bulk contact.

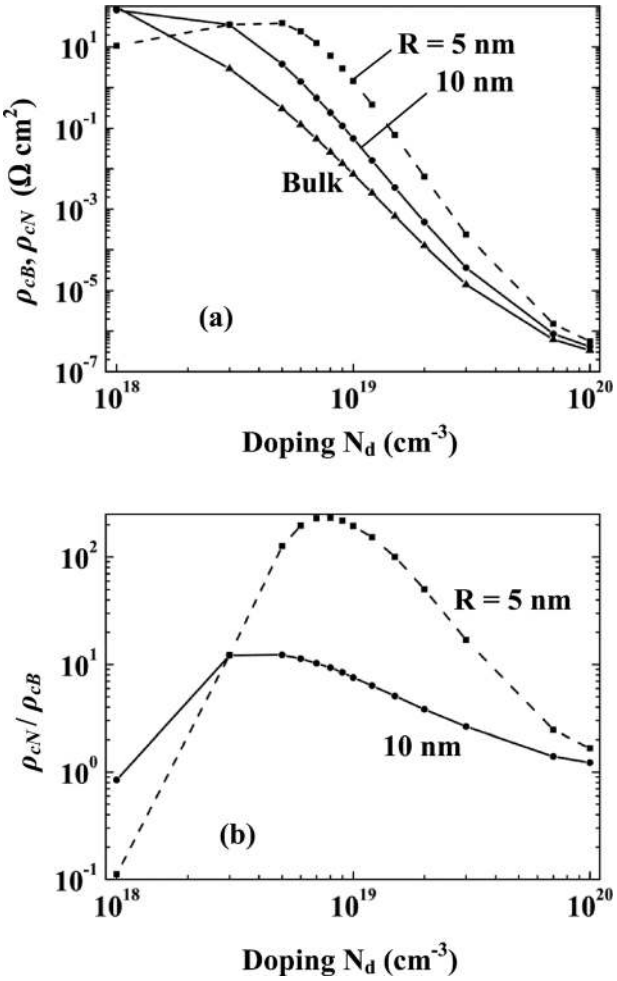

FIG. 2. (a) TCAD simulated doping dependence of the contact resistivity ρ_{cB} of bulk contacts and ρ_{cN} of nanowire contacts. Both contacts are to silicon and have $T = 300$ K, $\phi_{b0} = 0.8$ V, and $m = 0.3m_0$; nanowire contact has $\varepsilon_d/\varepsilon_0 = 3.9$ (SiO_2), $L_E = 350$ nm, $L_P = 0$ nm, $Q_s/q = 0$ cm^{-2}, and $s = 2.5 \times 10^5$ cm/s leading to $\tau_N = 1$, 2 ps for $R = 5$, 10 nm; bulk contact has $\tau_B = 1\,\mu$s. (b) Doping dependence of the ratio ρ_{cN}/ρ_{cB} obtained from (a).

Emission (FE). Another consequence of the higher space-charge width is a lesser junction electric field, resulting in lesser image force barrier lowering, $\Delta\phi$, and hence higher effective barrier height, $(\phi_{b0} - \Delta\phi)$, in the NW contact, where ϕ_{b0} is the intrinsic barrier height of both contacts. This widens the difference between I_T of the two contacts. The current density, J, and $\Delta\phi$ are non-uniform over the NW cross-section because of the non-uniformity of the space-charge width over the cross-section.

Nanodevices are being fabricated in NWs with progressively smaller R. In this paper, we discuss a realistic calculation of the contact resistivity, ρ_{cN}, of an *end-bonded* metal contact on *thin* n-type NW [see Fig. 1(a)] with R, as small as 5–10 nm,[4,13,19] which causes a strong surrounding field, dielectric confinement, and surface effects, for practical NW doping levels[1–3,5,13,20,21] of $10^{18} \leq N_d \leq 10^{20}$ cm^{-3} in the contact region. Our calculation includes I_T, I_{TE}, and I_{GR} [see Fig. 1(c)], where TE refers to Thermionic Emission. These currents are determined taking into account all the effects stated above, namely, surrounding field, charges and recombination at the NW surface, dielectric confinement, and image force barrier lowering; heavy doping effects of Fermi-Dirac statistics, impurity band formation, and bandgap narrowing are also considered. We do not consider quantum confinement effects since these are negligible[8,13] for $R \geq 5$ nm in silicon NWs.

For example, Fig. 2(a) shows our calculations of the N_d dependence of ρ_{cN} and its bulk counterpart ρ_{cB} for a contact on silicon NW surrounded by SiO_2 dielectric. Figure 2(b) shows the ratio ρ_{cN}/ρ_{cB}, which we study for the following reasons. ρ_{cB} (or ρ_{cN}) of junctions with the same N_d fabricated using different processes and laboratories can differ, e.g., see measured ρ_{cB} data of Refs. 22 and 23 given later in this paper and ρ_{cN} data of Ref. 5. Moreover, for the same junction, the value of ρ_c extracted using different methods can differ too. However, when ρ_{cN} and ρ_{cB} correspond to similar processes or extraction procedures, the process and measurement

related variations in ρ_{cN} and ρ_{cB} cancel each other out in their ratio ρ_{cN}/ρ_{cB}, which is expected to depend on device physics alone. Also, a model of ρ_{cN}/ρ_{cB} allows one to predict ρ_{cN} if ρ_{cB} is known from measurements or available models.[22,24]

Three features of the ρ_{cN}/ρ_{cB} versus N_d behavior of Fig. 2(b) are noteworthy: ρ_{cN}/ρ_{cB} is $\ll 1$ at $N_d = 1\times10^{18}\,\mathrm{cm}^{-3}$, reaches a peak $\gg 1$, and falls to ~ 1 at $N_d = 1\times10^{20}\,\mathrm{cm}^{-3}$. We explain these hitherto unreported features and study the ρ_{cN}/ρ_{cB} versus N_d behavior for different values of R, L_E, L_P, ε_a, Q_S, τ_N, ϕ_{b0}, temperature—T, and tunneling mass—m. We establish how the peak of a ρ_{cN}/ρ_{cB} versus N_d curve rises as we decrease T, m, R, L_P, or Q_S, or increase ϕ_{b0}, τ_N, L_E or ε_a. In contrast to our extensive numerical study reported in this paper, the existing numerical study[4] for metal contacts on GaAs NWs was limited to a single value of $N_d = 5\times10^{17}\,\mathrm{cm}^{-3}$ and air ambient; it reported a $\rho_{cN}/\rho_{cB} < 5$ for $R = 8$ nm at 300 K and did not consider the effects of I_{GR}, $\Delta\phi$, Q_S, and dielectric confinement.

Section II discusses the definition of contact resistivity which works irrespective of whether the current density over the contact area is uniform as in bulk contacts or non-uniform as in NW contacts. Section III explains the behaviors of ρ_{cN} and ρ_{cN}/ρ_{cB} versus N_d qualitatively. Section IV gives the equations and boundary conditions used for numerical simulations of charge, potential, and current distributions which yield the contact resistivity, also discussed is the calibration of the simulation set-up. Section V presents the calculated variation of ρ_{cN} and ρ_{cN}/ρ_{cB} versus N_d for a variety of conditions and explains this variation.

II. RESISTIVTY OF NANOWIRE CONTACTS

A theoretical definition of metal to semiconductor contact resistivity is given in Ref. 25 as $\rho_c = [dJ/dV|_{V\to0}]^{-1}$, where it is implicitly assumed that the current density, J, is uniform over the contact area. This definition is not suitable for contacts to NWs, where J inside the NW varies radially due to the variation in the space-charge width over the NW area arising from the effects of the surrounding field or surface charge [see Fig. 1(a)]. In spite of this limitation, some previous works[3,4] on NWs have used this definition by approximating J to be uniform. While this approximation may work for the values of N_d and R considered therein,[3,4] it breaks down at doping levels $> 1\times10^{19}\,\mathrm{cm}^{-3}$ and $R = 5$–10 nm, used in our work. Hence, we employ an alternate definition available in the literature,[5] namely, $\rho_c = [dI/dV|_{V\to0}]^{-1}A_c$, where I is the total current through the junction area A_c, and hence, J can be non-uniform. For end-bonded contacts to NWs considered in our work,

$$\rho_{cN} = \left[dI/dV|_{V\to0}\right]^{-1}\pi R^2. \tag{1}$$

III. CONTACT RESISTIVITY VERSUS DOPING—QUALITATIVE EXPLANATION

As mentioned in the introduction, components of current through metal contacts on heavily doped semiconductors are I_{TE}, I_T, and I_{GR}, where I_T includes TFE and FE [see Fig. 1(c)].

First, consider I_T. This current increases rapidly as N_d is raised since the space-charge width falls. Hence, in the N_d range of 1×10^{18}–$1\times10^{20}\,\mathrm{cm}^{-3}$ considered in this paper, I_T is significant in both bulk and NW contacts although it is much less in the latter because of the larger space-charge width due to the surrounding field effects.[4] Next, consider I_{GR}. In bulk contacts, I_{GR} is insignificant unless ϕ_{b0} is very large or τ_B is very low.[26] However, in NW contacts, I_{GR} is significant because τ_N is orders of magnitude smaller than τ_B, and in addition, the space-charge width is higher. Finally, as far as I_{TE} is concerned, it is independent of the space-charge width and hence the same in bulk and NW contacts having the same ϕ_{b0} (neglecting the differences in $\Delta\phi$ of the two contacts). However, in the N_d range considered in this paper, I_{TE} gets dominated by I_T in bulk contacts and $(I_{GR}+I_T)$ in NW contacts.

The above arguments imply that in Fig. 2(a), the ρ_{cB} versus N_d behavior can be explained in terms of I_T alone, while ρ_{cN} versus N_d behavior can be explained in terms of $(I_{GR}+I_T)$, considering bulk and NW contacts of the same area. As N_d is increased, the space-charge width falls, causing a rapid rise in I_T and a decrease in I_{GR}. Since ρ_{cB} is governed by I_T alone, it falls steadily over the entire N_d range. On the other hand, ρ_{cN} is governed by I_{GR} in the lower doping range, where the high space-charge width suppresses I_T and by I_T in the higher doping range, where the smaller space-charge width enhances I_T. Hence, as N_d is raised, for $R = 5$ nm, ρ_{cN} shows a rise due to the fall in I_{GR} followed by a rapid fall (like ρ_{cB}) due to the rapid rise of I_T. For $R = 10$ nm, the rising portion of ρ_{cN} flattens and changes to a slow fall; this is because, reduction in the surrounding field effect reduces the space-charge width, which reduces I_{GR} (which falls with N_d) and increases I_T (which rises with N_d) flattening the variation of $(I_{GR}+I_T)$. A similar change in the shape of ρ_{cN} versus N_d is observed if surrounding field effects are reduced by reducing ε_a.

We now explain the peaked behavior of ρ_{cN}/ρ_{cB} versus N_d, as shown in Fig. 2(b). At $N_d = 1\times10^{18}\,\mathrm{cm}^{-3}$, the current in the NW contact, which is due to I_{GR}, is $\gg$ the current in the bulk contact, which is due to I_T; hence, $\rho_{cN}/\rho_{cB} \ll 1$. At higher doping levels, I_T dominates in the NW contact, and since the current in the bulk contact is due to I_T as well, we have $\rho_{cN}/\rho_{cB} = I_{TB}/I_{TN}$, where I_{TB} and I_{TN} are values of I_T in bulk and NW contacts. In the doping range where the space-charge width in the NW contact is much higher than that in the bulk contact, $I_{TB}/I_{TN} \gg 1$ causing ρ_{cN}/ρ_{cB} to rise to values $\gg 1$. However, as $N_d \to 1\times10^{20}\,\mathrm{cm}^{-3}$, the surrounding field effects tend to vanish as lateral penetration of the surrounding field into the NW, characterized by Debye length $\propto N_d^{-1/2}$, is small. Under these conditions, the space-charge width over most of the NW contact area, except near the NW surface, is almost the same as that in the bulk contact (see Fig. 3), causing I_{TB}/I_{TN} and hence ρ_{cN}/ρ_{cB} to fall towards unity for $N_d \to 1\times10^{20}\,\mathrm{cm}^{-3}$.

We anticipate the following variations for the peak of ρ_{cN}/ρ_{cB} based on the above fact that this peak lies in the tunneling dominated regimes of NW and bulk contacts and originates from the difference in I_{TB} and I_{TN} due to the difference in the space-charge widths of the two contacts. Factors

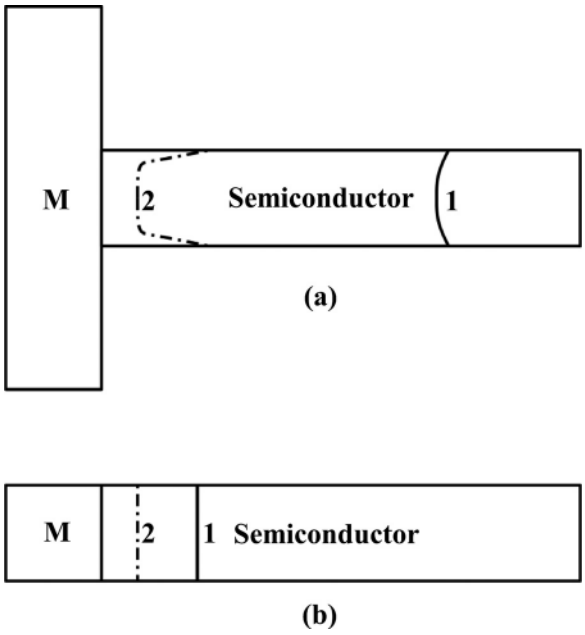

FIG. 3. The width and edge contour of the space-charge regions of a nanowire contact (a) and a bulk contact (b) at low doping (1) and high doping (2). See Fig. 1 for the charge and field pictures.

which suppress the surrounding field reduce the difference in space-charge widths and hence in the ratio I_{TB}/I_{TN}, lowering the peak; such factors include the increase in quantities, namely, R, L_P, or positive Q_S in n-type NW or reduction in L_E or ε_a. On the other hand, the difference in space-charge widths causes factors such as lower T, lower m, or higher ϕ_{b0} to reduce I_{TN} much more than I_{TB}, raising the peak. Another factor which raises the peak is increased τ_N, which reduces I_{GR} and hence enhances ρ_{cN} in the lower doping range. The factors affecting the peak also change ρ_{cN}/ρ_{cB} at low N_d.

Below, we undertake a quantitative study of the ρ_{cN}/ρ_{cB} versus N_d behavior including the above changes in the values at the peak and at low N_d. To get realistic results, we take into account a number of effects and factors stated in the introduction. Considering the number and complexity of mathematical equations required for this purpose, we resort to numerical simulations based on TCAD (Technology Computer Aided Design) Sentaurus[27].

IV. EQUATIONS AND BOUNDARY CONDITIONS USED IN SIMULATIONS

Using 2-D cylindrical simulations, we get I through the contact for a reverse bias $V =$ thermal voltage, V_t, and estimate $\rho_c = [dI/dV|_{V\to 0}]^{-1}\pi R^2 \approx [I/V|_{V=V_t}]^{-1}\pi R^2$, where $I \approx I_{GR} + I_T$ in NW contacts and $\approx I_T$ in bulk contacts.

A. Simulation of I_{GR} and I_T

The simulator solves numerically the five differential equations, namely, Poisson's equation, the drift-diffusion current density equations, and continuity equations for electrons and holes. Poisson's equation is solved inside the semiconductor in the bulk junction. However, in the NW junction, Poisson's equation is solved inside the NW and Laplace's equation is solved in the dielectric surrounding the NW.

I_{GR} in silicon NWs is estimated using the SRH theory as per which the net generation rate in the continuity equations for electrons and holes is given by

$$G_{SRH} = \frac{n_i^2 - np}{\tau_p\left[n + n_i\exp(E_{trap}/kT)\right] + \tau_n\left[p + n_i\exp(-E_{trap}/kT)\right]}. \quad (2)$$

Here, p denotes the hole density, n is the electron density, n_i is the intrinsic carrier concentration, E_{trap} is the energy difference between the defect level and the intrinsic level, and τ_n and τ_p are the electron and hole lifetimes. Our work assumes $E_{trap} = 0$ eV and $\tau_n = \tau_p = \tau_B = 1\ \mu$s in bulk contacts. For NW contacts, we use $\tau_n = \tau_p = \tau_N$ which is derived from the following formula

$$\tau_N = \left(\tau_B^{-1} + 2s/R\right)^{-1}. \quad (3)$$

Using $s = 2.5 \times 10^5$ cm/s based on the value extracted from measurements in Ref. 3, we get $\tau_N = 1$ and 2 ps for $R = 5$ and 10 nm.

I_T is estimated using the non-local electron tunneling model employed in Sentaurus;[27] hole tunneling is ignored. As per this model, the tunneling rate between the junction and a point, in a direction perpendicular to the junction area, is represented as a net generation rate G_T in the electron continuity equation.[28] G_T is calculated using the conduction band (E_c) profile, the local electron quasi-Fermi level E_{fs}, metal quasi-Fermi level E_{fm}, electric field E_{tun} in the direction of tunneling current, and the tunneling probability Γ as

$$G_T = \frac{A^*T^2}{qV_t}E_{tun}\,\Gamma(r,z)\ln\left(\frac{1+\exp\left[(E_c - E_{fs})/qV_t\right]}{1+\exp\left[(E_c - E_{fm})/qV_t\right]}\right), \quad (4)$$

where A^* is Richardson's constant and q is the electronic charge; $\Gamma(r, z)$ is obtained from the potential distribution between the junction and the point of calculation using WKB approximation

$$\Gamma(r,z) = \exp\left(\frac{-4\pi\sqrt{2m}}{h}\int_0^z \sqrt{E_c(r,p) - E_c(r,z)}\,dp\right), \quad (5)$$

where r and z represent the radial and axial coordinates, h is Planck's constant, and tunneling is from $(r, 0)$ to (r, z). In the present work, we assumed a doping and temperature independent tunneling effective mass $m = 0.3m_0$ for silicon[23] and $0.2m_0$ for GaN[5].

Since metal contacts are usually made to heavily doped semiconductor regions to reduce ρ_c, we included the heavy doping effects of partial impurity ionization, spreading of an impurity level into a band, Fermi-Dirac statistics, and bandgap narrowing (as per Slotboom's model[27]). The ionization energy $E_{ion} = E_c - E_d$, where E_d is the donor level, to be used to predict the impurity ionization including the dielectric confinement effect in NWs and impurity band formation, is estimated using[13–15]

$$E_{ion} = E_{ion0}(N_d) + \frac{2\varepsilon_0}{R\varepsilon_s}\left(\frac{x-1}{x+1}\right) \times \left(\frac{200.674 + 175.739x + 17.395x^2 + 0.0949x^3}{219.091 + 50.841x + x^2}\right), \quad (6)$$

where[27]

$$E_{ion0}(N_d) = E_{ion0}(0) - 3.1 \times 10^{-8} N_d^{1/3} \quad (7)$$

is the doping dependent ionization energy in bulk (in eV when N_d is in cm^{-3}), $x = \varepsilon_s/\varepsilon_a$, ε_0 is the permittivity of free space, and the numbers in the numerator in brackets have the units of eV-nm. The doping dependence of E_{ion0} is an effective representation of impurity band formation; the carrier concentration determined using E_{ion0} turns out to be the same as that determined by considering impurity band formation. For example, for the phosphorus dopant in silicon NW of $R = 5$ nm, E_{ion0} (0) = 45 meV, and for the SiO_2 (air) ambient, E_{ion} (0) = 85 (190) meV and E_{ion} = 55 (160), 18 (123), and −59 (46) meV for $N_d = 10^{18}$, 10^{19}, and 10^{20} cm^{-3}.

In our study, models for mobility are not as critical as those of the generation rate and tunneling since the current is not limited by drift-diffusion in the semiconductor neutral region. We include only the doping dependence of mobility (as per Masseti's model[27]).

B. Boundary conditions

First, we state the boundary conditions at the metal-semiconductor junction. The potential is taken as the sum of built-in potential and applied reverse bias, implying thereby that the potential is zero far away from the junction. The electron density n at this junction is derived from the following equations of the TE—diffusion theory[25] (analogous equations apply for holes)

$$J_{n\perp} = qv_n(n - n_s), \quad (8)$$

$$n_s = N_c \exp\left[-(\phi_{b0} - \Delta\phi)/V_t\right]. \quad (9)$$

Here, $J_{n\perp}$ is the normal component of electron current density calculated as discussed above, N_c is the effective density of states in the conduction band; v_n is the effective electron recombination velocity estimated using[25] $v_n = \sqrt{qV_t/(2\pi m_0 A^*/A_0)}$, where $A^* = 270$ A $cm^{-2}K^{-2}$ (for silicon) and m_0 and $A_0 = 120$ A $cm^{-2}K^{-2}$ are the mass and Richardson constant for free electrons; $v_n = 1.8 \times 10^6$ cm/s at $T = 300$ K for silicon. The image force barrier lowering $\Delta\phi$ is given by

$$\Delta\phi = \sqrt{qE/4\pi\varepsilon_s}, \quad (10)$$

where E is the junction field.

Next, we state the boundary conditions along the NW surface. Across this surface, the tangential electric field is continuous and the normal displacement vector is discontinuous by an amount equal to Q_s. The electron and hole current density normal to this surface are zero.

C. Simulator calibration

To calibrate our I_{GR} simulation approach, we compared our simulations of the effective generation width in the space-charge region for a reverse bias of V_t employed in our work with those reported in Ref. 17. This width corresponds to the part of the space-charge region where the electron and hole concentrations are less than the intrinsic concentration. As per Ref. 17, the ratio of this width to the depletion width in a p^+n silicon diode with parameters—(N_a, N_d) = (10^{19}, 10^{18} cm^{-3}), (τ_n, τ_p) = (1.0, 0.1 μs) is 1.78% at 300 K; the corresponding value in our simulations is 1.48%. When one of the parameters, N_d, is changed to 10^{14} cm^{-3}, Ref. 17 predicts the ratio to be 3%, while our simulations yield 3.3%. Thus, our simulations are within 10%–17% of the values reported in Ref. 17. Simulations show no change in the ratio when (τ_n, τ_p) is changed to (1, 1 μs) or (1, 1 ps).

The 10%–17% difference occurring in the calculation of I_{GR} leads to an equal difference in ρ_{cN} at lower doping levels $\sim 10^{18}$ cm^{-3}, where ρ_{cN} is governed by I_{GR} as explained in Sec. III. Such a variation in ρ_{cN} is imperceptible in the context of orders of magnitude variation of ρ_{cN} over the doping range of interest [see Fig. 2(a)]. Moreover, the 10%–17% difference has no impact on the bulk contact resistivity, ρ_{cB}, which as we explained in Sec. III is governed by tunnelling current, I_T, rather than I_{GR}.

We calibrated our I_T simulation approach using bulk contacts in two ways. We confirmed that our simulations reproduce the values of ρ_{cB} reported in Ref. 4 for $\phi_{b0} = 0.4$, 0.6, and 0.8 V at 300 K. In addition, Fig. 4 compares our ρ_{cB} simulations with the measured ρ_{cB} of Al, Pt, and PtSi metal contacts to bulk n-silicon, reported in two separate works;[22,23] we used $\phi_{b0} = 0.8$ V for Al and 0.9 V for Pt, PtSi contacts as per Ref. 25. The simulated results are seen to agree reasonably with the measured data over a wide doping range of $10^{17} \le N_d \le 10^{20}$ cm^{-3} for temperatures of $T = 300$, 200, and 77 K.

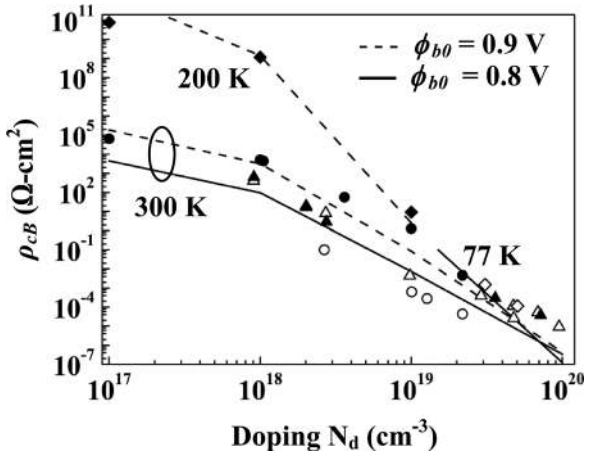

FIG. 4. Calibration of our TCAD simulations of bulk contact resistivity ρ_{cB} against the measured data in the literature for Al and Pt contacts on bulk n-type silicon. Lines show the simulation results, and points show the measured data from the literature. Legend: Δ Al 300 K, ◇ Al 77 K and ▲ Pt 300 K from Ref. 22; ○ Al 300 K, ● PtSi 300 K, and ◆ PtSi 200 K from Ref. 23.

V. RESULTS AND DISCUSSION

Figure 5 shows that ρ_{cN} versus N_d for $N_d < 5 \times 10^{18}\,\mathrm{cm}^{-3}$ is almost unaffected when ϕ_{b0} is raised from 0.8 to 1 V. This validates our observation in Sec. III that I_{GR} dominates over I_T at low N_d; had I_T been the dominant current, ρ_{cN} for $\phi_{b0} = 1$ V would have been much larger, as is the case with ρ_{cN} at higher doping levels or ρ_{cB} over the entire N_d range.

Figure 6 shows the simulated values of ρ_{cB} versus N_d under various conditions in one place to enable the estimation of ρ_{cN} from the ρ_{cN}/ρ_{cB} curves given in Figs. 2(b) and 7 discussed below.

A. Key overall trends of ρ_{cN}/ρ_{cB} versus doping

Consider the ρ_{cN}/ρ_{cB} versus N_d curve shown in Fig. 2(b) for parameter values, namely, $R = 5$ nm, $\phi_{b0} = 0.8$ V, $L_E = 350$ nm, $L_P = 0$, $\varepsilon_s = 12\varepsilon_0$, $\varepsilon_a = 3.9\varepsilon_0$, $Q_S = 0$, $\tau_N = 1$ ps, $T = 300$ K, and $m = 0.3m_0$. This is used as a reference for all comparisons below. Peak ρ_{cN}/ρ_{cB} is as high as 231 located at $N_d = 8 \times 10^{18}\,\mathrm{cm}^{-3}$, and $\rho_{cN}/\rho_{cB} = 0.1$ at $N_d = 1 \times 10^{18}\,\mathrm{cm}^{-3}$. This implies that for a metal contact on a sparsely packed NW array, the surrounding field can enhance ρ_{cN} significantly if the NW doping is $\sim 10^{19}\,\mathrm{cm}^{-3}$ and can reduce ρ_{cN} below ρ_{cB} by as much as 10 times due to surface generation-recombination if the NW doping is $\sim 10^{18}\,\mathrm{cm}^{-3}$. As anticipated, $\rho_{cN}/\rho_{cB} = 1.6$, i.e., approaches unity, at $N_d = 1 \times 10^{20}\,\mathrm{cm}^{-3}$.

Figures 2(b) and 7(a)–7(e) show the impact of varying one parameter at a time (from the above parameters of the reference curve) on ρ_{cN}/ρ_{cB} versus N_d behaviour. Before explaining each of these figures in detail, we note the following key overall patterns from them. Figure 7(a) shows that the reduction of L_E until 200 nm leaves the entire ρ_{cN}/ρ_{cB} versus N_d curve unchanged, implying that for a silicon NW of $R = 5$ nm, the surrounding field distribution saturates for $L_E > 200$ nm. This is why we have fixed L_E at 350 nm to study the effect of parameters other than L_E. Further, the ρ_{cN}/ρ_{cB} values near $N_d = 1 \times 10^{20}\,\mathrm{cm}^{-3}$ are almost unaffected for changes in any parameter other than the reduction in ε_a whose effect appears in Fig. 7(b). This is because at this high doping level, surrounding and surface fields altered by these parameters do not penetrate much into the NW (see Fig. 3), unless the ionized doping concentration is drastically reduced due to dielectric confinement which is stronger for lower ε_a. On the other hand, a significant change in any parameter affects the ρ_{cN}/ρ_{cB} values near $N_d = 1 \times 10^{18}\,\mathrm{cm}^{-3}$. This is because at this low doping level, surrounding and surface fields altered by these parameters penetrate into the NW affecting its space-charge width, and hence, the current and ρ_{cN}; changes in ϕ_{b0}, T, and m affect ρ_{cB}. More details of the ρ_{cN}/ρ_{cB} versus N_d curves, particularly the changes in the peak value and location, are now discussed one by one.

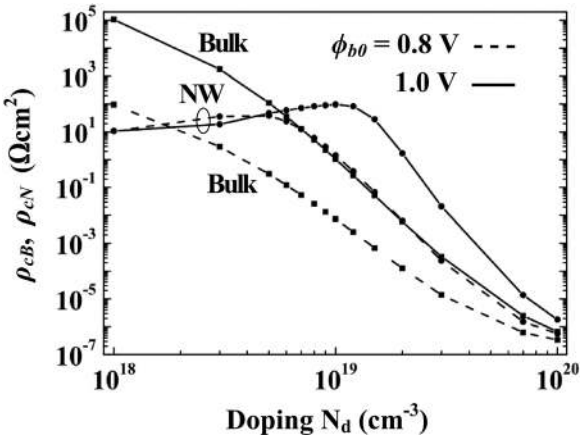

FIG. 5. Impact of barrier height ϕ_{b0} on the doping dependence of the TCAD simulated contact resistivity ρ_{cB} of bulk contacts and ρ_{cN} of nanowire contacts. Both contacts are to silicon and have $T = 300$ K and $m = 0.3m_0$; the nanowire contact has $R = 5$ nm, $L_E = 350$ nm, $L_P = 0$ nm, $\varepsilon_a/\varepsilon_0 = 3.9$ (SiO_2), $Q_s/q = 0\,\mathrm{cm}^{-2}$, and $s = 2.5 \times 10^5$ cm/s leading to $\tau_N = 1$ ps; the bulk contact has $\tau_B = 1\,\mu$s.

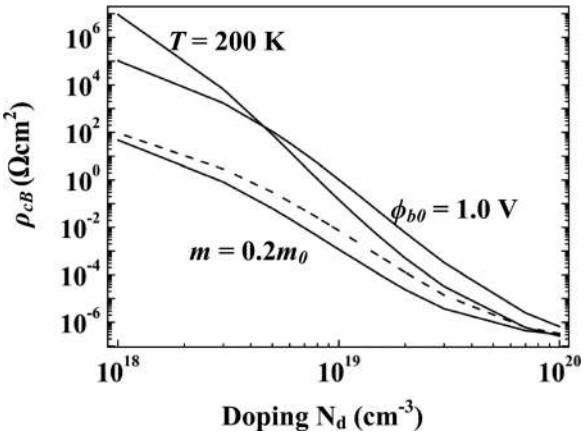

FIG. 6. TCAD simulated doping dependence of the contact resistivity ρ_{cB} of metal contacts to bulk silicon. The dashed curve corresponds to $\phi_{b0} = 0.8$ V, $T = 300$ K, $m = 0.3m_0$, and $\tau_B = 1\,\mu$s; other curves show the effect of varying T or m or ϕ_{b0}. These curves can be used to estimate ρ_{cN} from the ρ_{cN}/ρ_{cB} curves given in Figs. 2(b) and 7.

B. Effect of geometry

Consider the impact of reducing the surrounding field by raising R or L_P or lowering L_E. Figure 2(b) shows that increasing R from 5 nm to 10 nm flattens the curve as it should, suppressing the peak ρ_{cN}/ρ_{cB} from 231 to 12 and moving the values at extreme N_d towards unity. Although varying R changes dielectric confinement as per Eq. (6), this effect is negligible for the SiO_2 ambient, $\varepsilon_a = 3.9\varepsilon_0$ (discussed further later). Reduction of L_E below 200 nm [see Fig. 7(a)] reduces the peak without changing its location and moves the value at $N_d = 1 \times 10^{18}\,\mathrm{cm}^{-3}$ towards unity. It is noteworthy that the peak remains as high as 75 even for L_E as small as 10 nm. This means that, if the NW doping is $\sim 10^{19}\,\mathrm{cm}^{-3}$, the surrounding field will significantly enhance the ρ_{cN} of a metal contact, even if it is over a closely packed NW array, or if it is due to a thin probe on a single NW. On the other hand, a metal protrusion $L_P = 2R = 10$ nm brings the peak down to 63, implying that even a small penetration of the metal into NW or the presence of metallic nanoparticles during processing significantly reduce the surrounding field. It is seen that the metal protrusion does not affect ρ_{cN}/ρ_{cB} for $N_d < 3 \times 10^{18}\,\mathrm{cm}^{-3}$ since for such low N_d, the NW space-charge width $\gg L_P$.

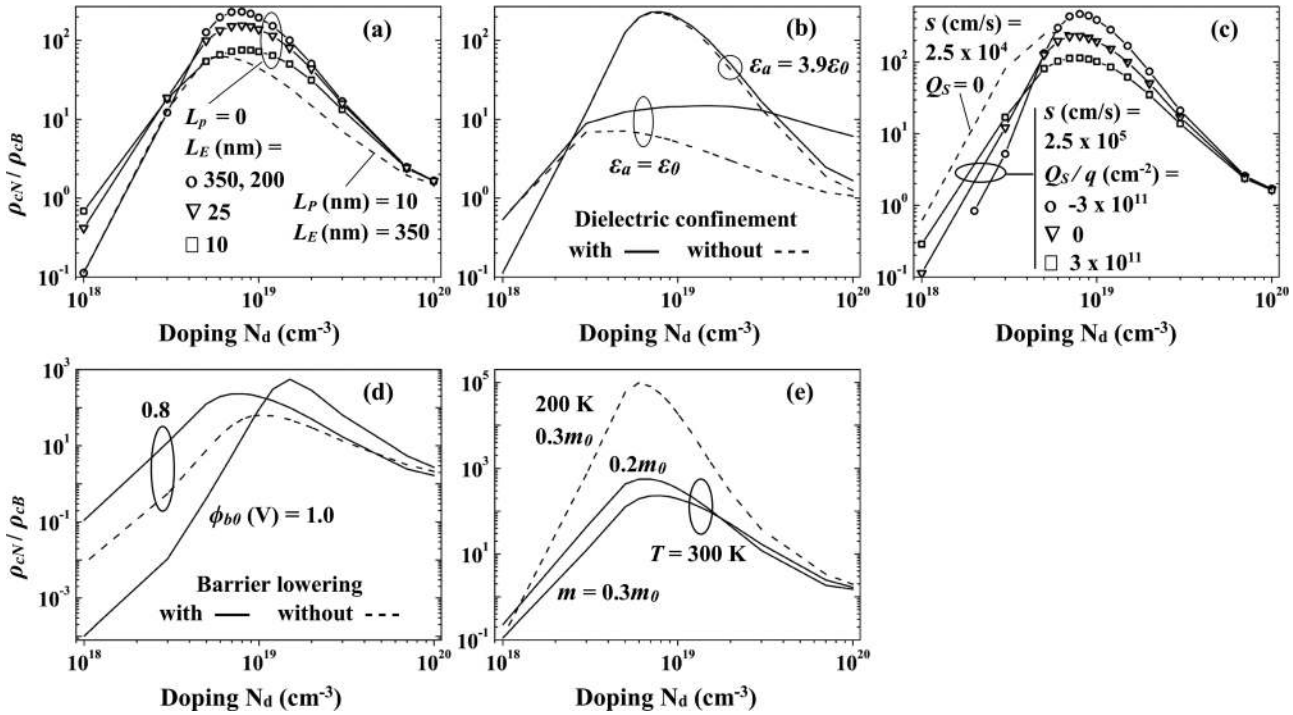

FIG. 7. Impact of various parameters on the TCAD simulated doping dependence of the ratio of the NW and bulk contact resistivities, ρ_{cN}/ρ_{cB}, for $R = 5$ nm. Parameters other than those shown in the figures are among the following: $L_E = 350$ nm, $L_P = 0$, $\varepsilon_a/\varepsilon_0 = 3.9$, $Q_s = 0$, $s = 2.5 \times 10^5$ cm/s, $\phi_{b0} = 0.8$ V, $T = 300$ K, $m = 0.3m_0$, and $\tau_B = 1$ μs. For $s = 2.5 \times 10^5$ and 2.5×10^4 cm/s, we get $\tau_N = 1$ and 10 ps.

C. Effect of the ambient dielectric

Consider the impact of reducing the surrounding field by lowering ε_a, which however increases the dielectric confinement at the same time, as per Eq. (6). In Fig. 7(b), for the air ambient ($\varepsilon_a = \varepsilon_0$), $\rho_{cN}/\rho_{cB} = 0.5$ at $N_d = 1 \times 10^{18}$ cm^{-3}, $= 15$ at the peak and $= 6$ at $N_d = 1 \times 10^{20}$ cm^{-3}, implying that the peak is rather broad and values at extremes of N_d are higher than those for the SiO_2 ambient. The fall of the peak and rise of ρ_{cN}/ρ_{cB} at $N_d = 1 \times 10^{18}$ cm^{-3} are due to the reduced surrounding field. However, the broadening of the peak and rise of ρ_{cN}/ρ_{cB} at $N_d = 1 \times 10^{20}$ cm^{-3} are due to increased dielectric confinement in NWs. This can be understood by comparing the ρ_{cN}/ρ_{cB} curves for the air ambient with and without dielectric confinement; this comparison essentially involves the comparison of ρ_{cN} since changes in ε_a do not affect ρ_{cB}. Inclusion of dielectric confinement increases E_{ion} at $N_d = 0$ from 45 meV to 190 meV for the air ambient. This does not affect ρ_{cN} for $N_d < 3 \times 10^{18}$ cm^{-3} where I_{GR} is the dominant current; I_{GR} depends on the space-charge width; this width does not change much with the increase in E_{ion} which simultaneously decreases the ionized doping concentration as well as the contact potential. For higher N_d, I_T begins to dominate. The decrease in I_T and hence the increase in ρ_{cN} as E_{ion} is increased can be reasoned as follows: Increased E_{ion} decreases the ionized N_d and hence the electron concentration in the neutral NW region, moving E_c in this region more and more above the Fermi-level. The energy location of peak emission associated with I_T has to be above the E_c of the neutral NW region. Hence, the rise of E_c implies the rise in the peak emission energy more and more above the metal Fermi-level, which in turn reduces I_T via the reduction of the Fermi-Dirac fraction at peak emission energy. Note that for the SiO_2 ambient, the curves with and without dielectric confinement almost coincide due to the smaller dielectric mismatch between NW and the ambient as compared to the air ambient case. Also, the features of the curve for $R = 5$ nm and the air ambient without dielectric confinement resemble those of the curve of Fig. 2(b) for $R = 10$ nm and the SiO_2 ambient, which corresponds to the reduced surrounding field as compared to $R = 5$ nm and negligible dielectric confinement (as pointed out above).

D. Effect of surface defects

Next, consider the surface effects, i.e., influence of Q_S [9–11] and s, depicted in Fig. 7(c). If Q_S/q is changed from 0 to -3×10^{11} cm^{-2}, the peak rises from 231 to 471 because of the increased junction space-charge width in NW required to provide the extra positive charge which neutralizes the negative Q_S. This increased space-charge width increases I_{GR}, thereby reducing ρ_{cN}/ρ_{cB} at lower N_d. By this logic, the reduced peak of 114 and higher ρ_{cN}/ρ_{cB} at lower N_d for a positive $Q_S/q = 3 \times 10^{11}$ cm^{-2} can be attributed to the reduced junction space-charge width. In all these cases, the peak location remains unaltered at $N_d = 8 \times 10^{18}$ cm^{-3}. If the value of s is decreased by a factor of 10 from 2.5×10^5 cm/s to 2.5×10^4 cm/s due to surface passivation, τ_N increases from 1 ps to 10 ps for $R = 5$ nm and I_{GR} is reduced. This increases ρ_{cN}/ρ_{cB} for low N_d and raises and shifts the peak to lower N_d marginally.

E. Effect of the barrier height

In Fig. 7(d), when ϕ_{b0} is increased from 0.8 V to 1 V, the peak increases from 231 to 557 (by a factor of 2.4) and its location shifts from $N_d = 8 \times 10^{18}\,\mathrm{cm}^{-3}$ to $1.5 \times 10^{19}\,\mathrm{cm}^{-3}$; also, ρ_{cN}/ρ_{cB} at $N_d = 1 \times 10^{18}\,\mathrm{cm}^{-3}$ falls steeply to 1×10^{-4} (by a factor of 1000), while that at $N_d = 1 \times 10^{20}\,\mathrm{cm}^{-3}$ increases marginally to 2.7. The increase in the peak is explained as follows. At the peak point, in both NW and bulk contacts, I_T dominates and an increase in ϕ_{b0} lowers the peak tunneling energy relative to the barrier top; this increases the difference in the tunneling distance and hence in the current between bulk and NW [see Fig. 1(c)]. At $N_d = 1 \times 10^{18}\,\mathrm{cm}^{-3}$, the steep fall in ρ_{cN}/ρ_{cB} is entirely because of the rise in ρ_{cB} due to the fall in I_T, while I_{GR} in NW and hence ρ_{cN} is almost unaffected (see Fig. 5).

We now explain why in Fig. 7(d), the neglect of $\Delta\phi$ reduces the peak from 231 to 63 (by a factor of 3) and the value at $N_d = 1 \times 10^{18}\,\mathrm{cm}^{-3}$ from 0.1 to 8.1×10^{-3} (by a factor >10), without affecting the value at $N_d = 1 \times 10^{20}\,\mathrm{cm}^{-3}$ as much. In the N_d range of 10^{18}–$10^{19}\,\mathrm{cm}^{-3}$, the bulk contact has a much lower space-charge width than the NW contact, leading to a higher junction field and hence a higher $\Delta\phi$ [see Fig. 1(c)]. Consequently, in this N_d range, with the neglect of $\Delta\phi$, the bulk contact experiences a higher increase in the effective barrier height, and correspondingly, a higher decrease in its current or increase in its ρ_c, leading to a fall in ρ_{cN}/ρ_{cB}. With the increase in N_d beyond $10^{19}\,\mathrm{cm}^{-3}$, the difference between the space-charge pictures of the two contacts and hence their $\Delta\phi$ decreases progressively and almost vanishes at $N_d = 1 \times 10^{20}\,\mathrm{cm}^{-3}$. Correspondingly, the difference between the curves with and without barrier lowering decreases progressively as N_d is increased.

F. Effect of temperature and tunneling mass

Figure 7(e) depicts the effect of reduction in T and in m. For these parameter changes, the peak tunneling energy relative to the barrier top is lowered. This increases the difference in the tunneling distance between bulk and NW [Fig. 1(c)], causing an increase in peak ρ_{cN}/ρ_{cB}. Changing T from 300 K to 200 K raises the peak from 231 to 9.8×10^4, and changing m from $0.3m_0$ to $0.2m_0$ (corresponding to GaN[5]) raises the peak from 231 to 564. The changes in T or m lower the peak location marginally from $0.8 \times 10^{19}\,\mathrm{cm}^{-3}$ to $0.6 \times 10^{19}\,\mathrm{cm}^{-3}$.

VI. CONCLUSION

We studied the doping dependence of the resistivity, ρ_{cN}, of end-bonded metal contacts to 10–20 nm thin semiconductor nanowires (NWs) having a heavy doping of 10^{18}–$10^{20}\,\mathrm{cm}^{-3}$. In this doping range, the resistivity, ρ_{cB}, of bulk contacts is governed by tunneling current and decreases steadily. However, up to 3–5 $\times 10^{18}\,\mathrm{cm}^{-3}$, ρ_{cN} is influenced by space-charge generation-recombination (GR) current since thin NWs with high surface recombination have a low effective lifetime; hence, ρ_{cN} varies slowly or may even increase. At higher doping levels, tunneling dominates and causes a steady fall in ρ_{cN} towards ρ_{cB} at $10^{20}\,\mathrm{cm}^{-3}$. The ratio ρ_{cN}/ρ_{cB}, which captures the surrounding field, surface, and dielectric confinement effects in the NW, can be $\ll 1$ at $10^{18}\,\mathrm{cm}^{-3}$ due to large GR current in the NW contact. At higher doping levels where tunneling dominates in both contacts, this ratio reaches a peak $\gg 1$ around $10^{19}\,\mathrm{cm}^{-3}$, where the space-charge width in the NW contact is much higher than that in the bulk contact due to the surrounding field effect, and falls towards unity at $10^{20}\,\mathrm{cm}^{-3}$, where space-charge pictures in the two contacts are similar. We reported realistic TCAD simulations of ρ_{cN}, ρ_{cB}, and ρ_{cN}/ρ_{cB} versus doping, including both tunneling and GR currents, impact of extension and protrusion of the contact metal, ambient dielectric and dielectric confinement, NW thickness, surface charge and recombination velocity, barrier height, barrier lowering, temperature, and tunneling mass. These simulations also incorporated heavy doping effects such as Fermi-Dirac statistics, bandgap narrowing, and impurity band formation. This study is useful for design and characterization of NW devices.

[1] F. Léonard and A. A. Talin, Nat. Nanotechnol. **6**, 773 (2011).
[2] C. Fernandes, A. Shik, K. Byrne, D. Lynall, M. Blumin, I. Savaliev, and H. E. Ruda, Nanotechnology **26**, 085204 (2015).
[3] F. Léonard, A. A. Talin, B. Swartzentruber, and S. Picraux, Phys. Rev. Lett. **102**, 106805 (2009).
[4] J. Hu, Y. Liu, C. Z. Ning, R. Dutton, and S. M. Kang, Appl. Phys. Lett. **92**, 083503 (2008).
[5] E. Stern, G. Cheng, M. P. Young, and M. A. Reed, Appl. Phys. Lett. **88**, 053106 (2006).
[6] X. L. Han, G. Larrier, E. Dubois, and F. Cristiano, Surf. Sci. **606**, 836 (2012).
[7] D. Erts, B. Polyakov, B. Daly, M. A. Morris, S. Ellingboe, J. Boland, and J. D. Holmes, J. Phys. Chem. B **110**, 820 (2006).
[8] V. K. Gurugubelli and S. Karmalkar, J. Appl. Phys. **119**, 024507 (2016).
[9] V. Schmidt, S. Senz, and U. Gösele, Appl. Phys. A **86**, 187 (2007).
[10] I. Kimukin, M. S. Islam, and R. S. Williams, Nanotechnology **17**, S240 (2006).
[11] K. Seo, S. Sharma, A. A. Yasseri, D. R. Stewart, and T. I. Kamins, Electrochem. Solid State Lett. **9**, G69 (2006).
[12] P. Agarwal, M. Vijayaraghavan, F. Neuilly, E. Hijzen, and G. Hurkx, Nano Lett. **7**, 896 (2007).
[13] V. Schmidt, J. V. Wittemann, S. Senz, and U. Gösele, Adv. Mater. **21**, 2681 (2009).
[14] Y. M. Niquet, A. Lherbier, N. H. Quang, M. V. Fernandes-Serre, X. Blase, and C. Delerue, Phys. Rev. B **73**, 165319 (2006).
[15] M. Diarra, Y. M. Niquet, C. Delerue, and G. Allan, Phys. Rev. B **75**, 045301 (2007).
[16] V. K. Gurugubelli and S. Karmalkar, Appl. Phys. Lett. **104**, 203502 (2014).
[17] P. U. Calzolari and S. Graffi, Solid-State Electron. **15**, 1003 (1972).
[18] E. C. Garnett and P. Yang, J. Am. Chem. Soc. **130**, 9224 (2008).
[19] L. Li, Y. Fang, C. Xu, Y. Zhao, N. Zang, P. Jiang, and K. J. Ziegler, Nanotechnology **27**, 165303 (2016).
[20] S. A. Dayeh, R. Chen, Y. G. Ro, and J. Sim, Mater. Sci. Semicond. Process. **62**, 135 (2017).
[21] H. Schmid, M. T. Bjork, J. Knoch, S. Karg, H. Riel, and W. Riess, Nano Lett. **9**, 173 (2009).
[22] A. Y. C. Yu, Solid-State Electron. **13**, 239 (1970).
[23] C. Y. Chang, Y. K. Fang, and S. M. Sze, Solid-State Electron. **14**, 541 (1971).
[24] H. Park, R. Beresford, S. Hong, and J. Xu, J. Appl. Phys. **108**, 094308 (2010).
[25] S. M. Sze and K. K. Ng, *Physics of Semiconductor Devices* (Wiley India, New Delhi, 2007).
[26] B. J. Baliga, *Modern Power Devices* (John Wiley & Sons, NY, 1987), p. 428.
[27] Synopsys, *Sentaurus Device User Guide* (Synopsys, 2015).
[28] M. Ieong, P. M. Solomon, S. E. Laux, H.-S. P. Wong, and D. Chidambarrao, in *International Electron Devices Meeting Technical Digest* (1998), p. 733.